Separation of instrumental and astrophysical foregrounds for mapping CMB anisotropies

J. Delabrouille[1], G. Patanchon[1] & E. Audit[2]

[1] *PCC — Collège de France, 11, place Marcelin Berthelot, F-75231 Paris, France*
[2] *CEA/DSM/DAPNIA Service d'Astrophysique, CEA/Saclay 91191 Gif-sur-Yvette Cedex, France*

ABSTRACT

For the most sensitive present and future experiments dedicated to Cosmic Microwave Background (CMB) anisotropy observations, the identification and separation of signals coming from different sources is an important step in the data analysis. This problem of the restitution of signals from the observation of their mixture is classically called "component separation" in CMB mapping. In this paper, we address the general problem of separating, for millimeter-wave sky mapping applications, components which include not only astrophysical emissions in two-dimensional maps, but also one-dimensional instrumental effects in the data streams. We show that component separation methods can be adapted to separate simultaneously both astrophysical emissions and components coming from time-dependent foreground signals originating from the instrument itself. Such general methods can be used for the optimal processing of low-redundancy observations where multi-channel observations are a precious tool to remove systematic effects, as may be the case for the Planck mission.

Key words: Cosmic microwave background – Cosmology: observations – Methods: data analysis

1 INTRODUCTION

Mapping and interpreting sky emissions in the millimeter and sub-millimeter range, and in particular Cosmic Microwave Background (CMB) temperature anisotropies, is one of the main objectives of present and upcoming observational effort in millimeter-wave astronomy. This is, in particular, the objective of balloon and space–borne missions as Archeops (Benoît et al. 2001), Boomerang (de Bernardis et al. 1999), Maxima (Hanany et al. 2000), TopHat (Silverberg 2000), MAP (Wright 1999) and Planck (Lamarre et al. 2000; Bersanelli et al. 2000). Among the scientific objectives of these missions, the precise measurement of primordial temperature and/or polarisation fluctuations of the CMB is one of the priorities.

The importance of measuring anisotropies of the Cosmic Microwave Background (CMB) to constrain cosmological models is now well established. In the past ten years, tremendous theoretical activity, motivated by upcoming ambitious balloon-borne and space missions, demonstrated that measuring the properties of these temperature anisotropies will constrain drastically the seeds for structure formation as well as the cosmological parameters describing the matter content, the geometry, and the evolution of our Universe (Hu & Sugiyama 1996; Jungman et al. 1996). The accuracies

required for precision tests of the cosmological models and measurements of the cosmological parameters (the Hubble constant H_0, the total matter density Ω_m, the cosmological constant Λ, . . .), however, is such that it is necessary to disentangle in the data the contribution of several distinct astrophysical sources, all of which emit radiation in the frequency range used for CMB observations, i.e. the 10 GHz - 800 GHz range.

This problem, now traditionnally called "component separation" by the CMB community, has been adressed already by a number of authors (Tegmark & Efstathiou 1996; Hobson et al. 1998; Bouchet & Gispert 1999; Bouchet, Prunet & Sethi 1999; Baccigalupi et al. 2000; Snoussi et al. 2001; Maino et al. 2001) using different assumptions and analysis techniques. It is a particular application of the problem of "source separation", also called in signal processing the "cocktail party" problem, in which a number of source signals (timestreams, images. . .) has to be recovered from the observation of their mixture in a number of captors.

So far however, only the separation of astrophysical components has been adressed using a component separation formalism. In addition, the separation has been implemented for ideal white noise on the observed maps. Real measurements however often suffer from instrumental effects, coloured noise, and involve the reprojection of one-

dimensional data streams onto somewhat irregularly sampled two-dimensional maps, where some pixels may be observed several times and/or others not covered at all by the observations, depending on the resolution of the reconstructed map. In this paper, we investigate the possibility to extend the Wiener solution discussed by Tegmark & Efstathiou (1996) and Bouchet & Gispert (1999) to deal also with instrumental foregrounds. We test the method in more realistic situations which include non-white detector noise and uncertainties induced by the reprojection of timelines.

The remaining of this paper is organised as follows: In section 2, we introduce the general formalism of component separation and discuss the possibilty to include instrumental components and their specificities. In section 3, we discuss the simulation of Planck observations containing the superposition of CMB and thermal dust emission, an instrumental effect, low-frequency detector noise, and white noise. In section 4, we discuss the Wiener method implemented to separate these components in the simulated Planck data, and show the results we obtain. In section 5, we discuss the results and the generality of the method. We conclude in the last section.

2   COMPONENT SEPARATION

One of the key aspects of the component separation is the exploitation of the presumably known (at least to a large extent) dependence of the component emission on the frequency of observation ν. Although it is not always necessary that the frequency scalings be known *a priori* (Baccigalupi et al. 2000; Snoussi et al. 2001; Maino et al. 2001), separation techniques rely on the existence of such a frequency scaling. In this framework, for multifrequency observations of the sky, the observed emission at frequency ν is the linear superposition of the emission of several components:

$$I(\vec{n}, \nu) = \sum_c I_c(\vec{n}, \nu) \qquad (1)$$

where $I_c(\vec{n}, \nu)$ stands for the emission of component c as a function of direction $\vec{n}$ and frequency ν. For each component, the emission can be well approximated as the product of a frequency spectrum $A_c(\nu)$ and a spatial template $\Delta(\vec{n})$.

$$I_c(\vec{n}, \nu) = A_c(\nu)\Delta_c(\vec{n}) \qquad (2)$$

This approximation is very good for small portions of the sky. For larger maps (especially covering both low and high galactic latitudes), there can be variations of the emission law of the galactic components.

The decomposition in equation 2 is not unique, as a multiplicative constant factor can be taken from A into Δ. For convenience, we adopt the convention that Δ_c is the 200 GHz template of component c in units of $\Delta T/T_{\mathrm{CMB}}$, that is:

$$\Delta_c(\vec{n}) = I_c(\vec{n}, 200\,\mathrm{GHz})\frac{1}{T_{\mathrm{CMB}}}\left[\frac{\partial B_\nu}{\partial T}(T_{\mathrm{CMB}}, 200\,\mathrm{GHz})\right]^{-1} (3)$$

with $T_{\mathrm{CMB}} = 2.726$ K, and B_ν is the Planck Blackbody spectrum.

For the present application, we will assume that the frequency spectra of astrophysical component emissions are known, which is a reasonable assumption in the 100-800 GHz

frequency range, where the sky emission at moderate galactic latitude is dominated by CMB anisotropies and thermal galactic dust emission (see figure 4). The CMB anisotropy spectrum is the derivative of a blackbody with respect to temperature:

$$A_{\mathrm{CMB}}(\nu) = \frac{\partial B_\nu}{\partial T}(T_{\mathrm{CMB}}, \nu) \qquad (4)$$

Thermal dust emission is well fitted in this frequency range by a thermal spectrum with a ν^2 emissivity and a temperature of 17.5 K:

$$A_{\mathrm{dust}}(\nu) = \left(\frac{\nu}{200\,\mathrm{GHz}}\right)^2 \frac{B_\nu(17.5\mathrm{K}, \nu)}{B_\nu(17.5\mathrm{K}, 200\,\mathrm{GHz})} \qquad (5)$$

This temperature of 17.5 K can change slightly (at the level of a few Kelvin) across the sky (Schlegel, Finkbeiner & Davies 1998), which is a motivation for a local treatment of component separation (as compared to full-sky methods).

In addition to the known frequency dependence, one can introduce priors on the spatial statistical properties of the foregrounds. For Gaussian random fields, exploiting the prior knowledge of the autocorrelation leads to methods as the Wiener solution implemented and tested on simulations by Tegmark & Efstathiou (1996) and Bouchet & Gispert (1999).

In addition to diffuse galactic and extragalactic components, several populations of point-like sources are expected to contribute to the microwave sky emission. Dedicated techniques are being developed for their extraction (Vielva et al. 2001). At this point however, techniques developed to separate components in CMB experiments did not address the problem of non-astrophysical components, i.e. of signal fluctuations in detector readouts that are not due to astrophysical emission, fixed on the sky, but to the physical emission of other objects radiatively, or conductively, coupled to the detectors.

One exemple of such a "foreground" is the thermal emission of a slightly emissive telescope which temperature fluctuates in time. Detectors experience a time-dependent additive fluctuation of their signals, which, reprojected on the sky according to each detector's specific scanning strategy in the process of recombining timelines into maps, generate fake position-dependent anisotropies on each detector's reconstructed sky map.

Another example, specific to bolometric detectors, is the signal generated by temperature fluctuations of the thermal bath required to cool the detectors to sub-kelvin temperatures. Such fluctuations have been seen in detector timelines for the Archeops Balloon test flight (Benoît et al. 2001), and are expected to be present (at a much lower level) in Planck HFI data as well.

Finally, one other interesting example is that of atmospheric emission for sub-orbital experiments, in which case time and space dependent fluctuations of the atmosphere temperature and composition in the line of sight generate fluctuations in the detectors timelines.

Because of the process of their generation, such foregrounds are seen by all detectors simultaneously. However, as fields of views of all detectors of a CMB experiment as the current ones do not point towards the same point of the sky at the same time, they cannot be treated as another component on the sky. It is a component which "lives" in the time domain, and which is reprojected on the sky according

to the scanning strategy, in a detector-dependent way. As a consequence, a given pixel on the sky, being observed at different times by different detectors, is not polluted by the same instrumental foreground for different detectors.

Quite often, such instrumental foregrounds are essentially low frequency drifts, although one might imagine scan-synchronous temperature fluctuations depending on the orientation of the experiment with respect to external sources of heat as the Sun, or line-spectra fluctuations induced by cyclic power dissipation or by vibrations within the experimental set-up (e.g. engines).

In the case of random slow drifts, a common way to handle this kind of systematics is simply to filter them out using a high-pass filter. This method has the merit of simplicity and efficiency, but reduces the sensitivity of the experiment to scales larger than $\omega_{scan} \times f_{filter}$, where ω_{scan} is the scanning speed on the sky and f_{filter} the filter cutout frequency. For experiments aiming at measuring anisotropies at all available scales, including the largest ones, more sophisticated destriping methods are implemented. Such methods, whatever the exact algorithm used, essentially rely on redundancies (i.e. coming back to the same point of the sky on different timescales) and some prior assumptions about the slow drifts. They are not efficient in removing fluctuations of the systematic effect on timescales smaller than the typical "redundancy timescale", unless they have built in some filter which effectively does the equivalent of a high-pass filter on the timelines.

For a scan strategy such as that of Planck, a timeline-processing destriping technique as that of Cottingham (1987) and Delabrouille (1998), which would non-destructively reproject "near-optimally" each single timeline onto a map of the sky while removing slow drifts of various origin, may be quite unefficient in removing stripes in regions near the ecliptic plane, simply because of a lack of redundancy (Delabrouille et al. 2000). The Planck scanning indeed is such that each detector's field of view scans the sky on large (~ 85 degree radius) circles centered near the ecliptic. The center of the circles is shifted by a few arcminutes every hour or so, the final field-of-view trajectory for each detector being a bundle of large circles intersecting each other near the ecliptic poles, with no intersection, or very few, in the region of the ecliptic (see figure 1).

In addition, removing correlated low-frequency drifts induced by the detector pickup of slow thermal fluctuations on the payload would be non-optimal, because it does not take advantage of the physical origin of the systematic which gives rise to correlations. Taking care of this by using map making techniques as adapted versions of MADCAP (Borrill 1999) which would treat all detectors simultaneously, taking into account noise (i.e. systematic effect) correlations is a possibility, but is very intensive computationnaly. In this paper, we investigate the option which consists in treating the time-domain systematic effect as another component, "living" in the time domain and not on two-D maps, taking care of the specificities this implies as compared to sky-attached, more traditionnal, astrophysical foregrounds.

3 SIMULATIONS

We now investigate specifically the separation of instrumental and astrophysical components on simulations tailored for the Planck mission. Much of the discussion can be straightforwardly adapted to other experiments as Archeops or Boomerang. The Planck mission, scheduled to be launched by ESA in 2007, will measure full-sky temperature and polarisation anisotropies of the sky emission in the frequency range 30 to 850 GHz. The data will be taken using two instruments, the Low Frequency Instrument (LFI), and the High Frequency Instrument (HFI). The LFI consists of 56 radiometers cooled to 20K, split into four frequency channels in the 30-100 GHz range (Mandolesi et al. 2000; Bersanelli et al. 2000), and the HFI of 48 bolometers split into 6 channels between 100 and 850 GHz (Lamarre et al. 2000). This large frequency coverage, associated to unprecedented detector sensitivity, will allow to measure microwave anisotropies with a final sensitivity of about 6 μK per 8 arcminute pixel, provided all systematic effects remain under control.

We will investigate a component separation method that could be used for this mission among others, restricting ourselves to two sky components (CMB and thermal dust emission), one low frequency time-domain systematic effect due to the pickup of thermal emission from a part of the instrument, and realistic noise, including both white noise (in the time domain) and low-frequency detector noise (with a knee frequency of 0.01 Hz, as expected for Planck HFI detectors). We will process the observations of the 48 HFI detectors only (6 channels) to avoid overconstraining excessively the problem. The method can be generalised to include LFI detectors as well, and more astrophysical (e.g. free-free emission, synchrotron, Sunyaev-Zel'dovich (SZ) effect (Sunyaev & Zel'dovich 1972), another dust component, zodiacal emission) or time-domain (e.g. temperature of reference load, thermal bath fluctuations) components.

We implement the method on small square maps located near the ecliptic plane, convenient for a Fourier processing of the data. The motivation for the choice of location is that in regions near the ecliptic poles, redundancies in the measurements are such that standard "optimal" map making or destriping methods may be sufficient to remove the systematic effect, whereas we do not anticipate that this will be the case near the ecliptic. We pick a region located at coordinates $\alpha = 204$ degrees and $\delta = 11$ degrees ($\lambda = 198$ degrees and $\beta = 19.5$ degrees), close to the ecliptic plane (for the scans to be almost parallel) and at a high galactic latitude (70 degrees). We choose, for the specific illustration of our discussion here, a 272×272 pixels square map with two sides parallel to the equator, and a pixel size of 2.5 arcminutes.

The scanning strategy we adopt for generating our data is close to one of the possible Planck scanning strategies. It consists in spinning the spacecraft at 1 RPM so that the beam axis, for each detector, scans the sky along large circles with 80 to 90 degrees angular radius (depending on the detector). The spin axis is held fixed for about an hour, so that each of the detector main beams scans the same circle on the sky about 60 times. Every hour, the spin axis is displaced by about 2.5 arcminutes to follow the apparent yearly motion of the Sun, and get a complete sky coverage in about 6 months. Figure 1 illustrates the Planck scanning
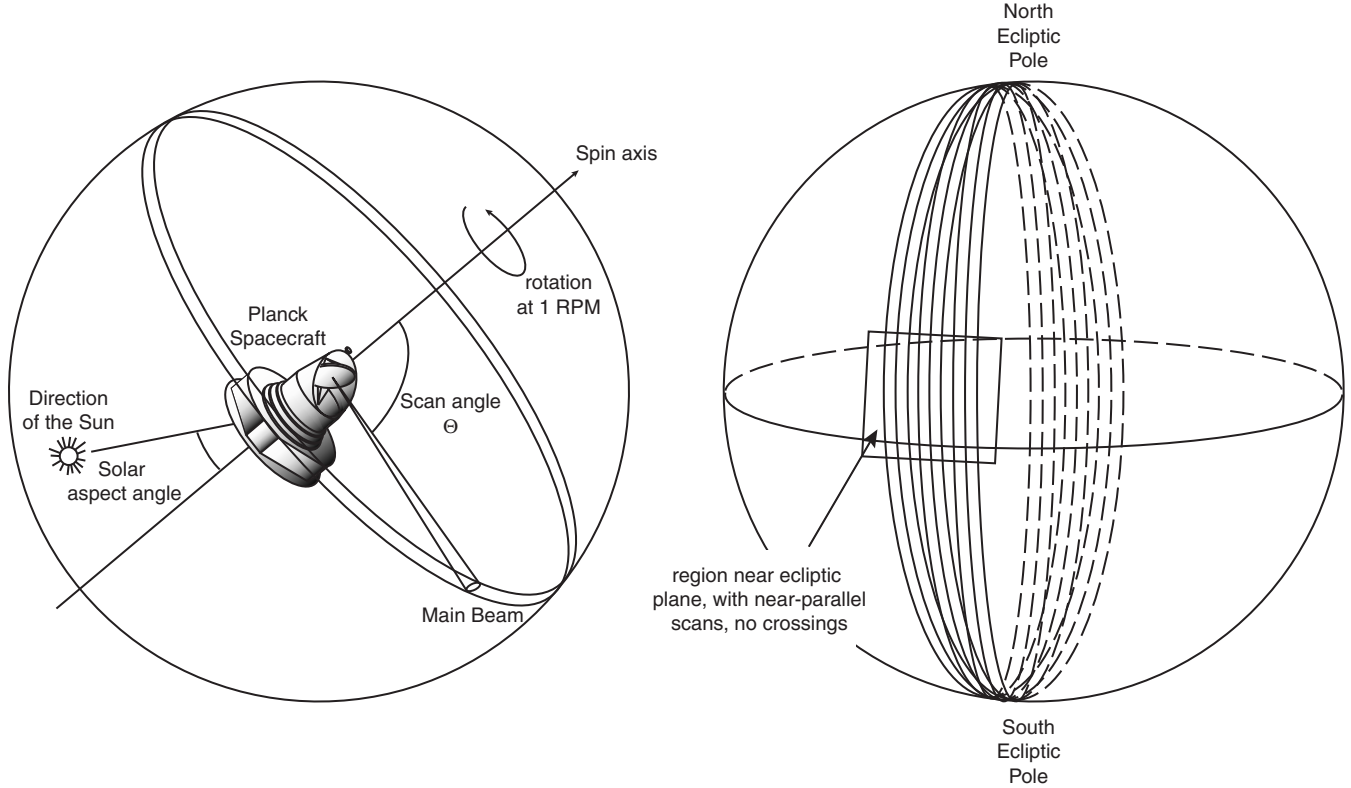
Figure 1. Illustration of the Planck scanning strategy. On the left panel, the trajectory of the field of view of one single detector is shown. On the right panel, we show the trajectories of the centers of the fields of views of three distinct detectors for three spin axis position of Planck. For adjacent spin axis positions, the trajectories of all detectors are close to parallel for pointings near the ecliptic plane.

strategy. Due to the detector setup in the focal plane, the scan-angle θ is slightly different for different detectors.

We now turn to generating synthetic observations of this region for all Planck HFI detectors, featuring CMB, dust, an instrumental effect, and detector noise.

3.1 Astrophysical components

The CMB component is a COBE-normalised, randomly generated realisation of CMB anisotropies obtained using C_ℓ predicted by the CMBFAST software (Seljak & Zaldarriaga 2000) for a Universe with $H_0 = 65$ km/s/Mpc, $\Omega_m = 0.3$, $\Omega_b = 0.045$, $\Lambda = 0.7$. The CMB anisotropy emission is scaled as a function of frequency using the temperature derivative of the Planck law at T=2.726 K.

The dust component is simply the extrapolation of the IRAS observed 100 micron map (bright stars removed) with an assumed emission proportional to $\nu^2 \times B_\nu (T = 17.5K)$. The sum of the two for each frequency channel gives the sky emission observable in that band in our simulation.

Input templates for CMB and dust emission can be seen in figure 5.

We observe the simulated maps assuming locally a parallel scanning strategy such that the scans are distant, for a given detector, of 2.5 arcminutes from each other. We adopt the focal plane geometry described in (Lamarre et al. 2000). For each detector, a purely astrophysical timeline is generated for each Planck detector by observing the properly weighted superposition of CMB and dust maps in a set of samples obtained each by integrating the sky emission in a symmetric Gaussian beam, properly positioned with respect to the map according to our selected scanning strategy. The beam size ranges from 10 arcminutes (at 100 GHz) to 5 arcminutes (at 857 GHz).

After this operation, we get a timeline in which only samples corresponding to observations in our generated map are non zero. At equal times, the 48 detectors do not point towards the same point on the sky because of the focal plane geometry. Shifts up to a few degrees, due to the angular extent of the image of the focal plane of the sky, separate the fields of views (FOVs) of the different detectors on the sky.

3.2 Systematic effect

A simulated instrumental foreground is generated in the form of a timeline corresponding to a plausible temperature fluctuation of an optical element: we generate a random, correlated gaussian stream, with a spectrum (as a function of frequency f) proportional to f^{-2}. This is quite typical of temperature fluctuations observed in other experiments. We assume that a prior timeline treatment as, e.g., that of Delabrouille (1998) has permitted the removal of the effect of such fluctuations on timescales larger than the spinning

frequency of Planck, corresponding to one revolution of the satellite (one minute of time for a 1 RPM scanning). In the end, the simulated instrumental effect due to temperature fluctuations has a $1/f^2$ spectrum between $f_{\mathrm{spin}} \simeq 0.017$ Hz and $f_{\mathrm{sampling}} \simeq 170$ Hz, and falls off to negligible values outside this interval.

The impact of the instrumental effect on each detector timeline depends on the value of a coupling coefficient for each detector. These coupling coefficients tells us how much the physical temperature fluctuations impact each detector reading. They depend on the emissivity properties of the object whose temperature fluctuates (as a function of frequency ν), and on the optical and geometrical properties of the setup. We assume here a $\nu^{5/2}$ dependence (close to the Rayleigh-Jeans limit of a greybody with emissivity proportionnal to $\sqrt{\nu}$ as expected typically in our frequency range for aluminium). The requirement on the temperature stability of the Planck payload, including the mirrors, is 0.2 mK. Such a temperature stability can be achieved in the very quiet space environment of the L2 Lagrange-point orbit of Planck, but not very easily for balloon-borne experiments as Archeops or Boomerang. For our simulation, we assume a pessimistic temperature fluctuation of about 1 mK RMS integrated on timescales between 0.017 Hz and 170 Hz (5 times higher than the expected upper limit for Planck), with the above $1/f^2$ spectrum and with a 3 % total emissivity at 200 GHz.

This assumption of a strong instrumental effect, above expectations for Planck, make the dust contribution subdominant in all frequency channels. This allows us to test the separation of a "weak" astrophysical component.

Note that no detector dependence of the coupling within a frequency band is assumed in our simulation. Such a dependence may exist in other cases as temperature fluctuations of a shield, for instance, where geometrical considerations have to be taken into account in the couplings.

3.3 Detector noise

For each detector, we generate a Gaussian coloured noise stream with a spectrum of the form $S_n(f) = K \times (1 + f_{\mathrm{knee}}/f)$, i.e. a typical detector noise with a white part and a $1/f$ part. The knee frequency (frequency at which the two parts contribute equally) is taken to be $f_{\mathrm{knee}} = 0.01$ Hz, which corresponds to laboratory measurements performed for the Planck HFI. The noise is assumed to be uncorrelated between detectors. Noise figures for the white noise level are representative of predictions for Planck HFI detectors. Again, we assume that very slow fluctuations have been removed, so that there remains no power outside the 0.017-170 Hz frequency band. One noise timeline is generated for each detector, and added to the appropriate data streams, which contain thus each the contributions from two astrophysical components, one instrumental component, and coloured noise.

3.4 Reprojection on sky maps

For convenience, we will perform our treatment on two-dimensional data rather than timelines. In the present implementation of the component separation, this allows to work easily in the Fourier space while taking into account the different detector pointings, in small regions of parallel scanning. We reconstruct a two-dimensional "observed" map for each detector by fitting to the observed timelines along with corresponding pointings a quintic surface defined in each pixel, matching best the observed data. A map of the systematic effect alone, obtained in the same way from the systematic effect timeline of a fictitious detector centered on the optical axis of Planck, is shown in figure 5.

In figure 2, we display the reconstructed observed maps for one single detector of each channel. These maps include the reprojected noise and systematic effect for each detector, as well as the observed astrophysical components. In figure 3, we display the observations for 3 detectors of the 217 GHz channel, which show the detector dependence of the observed systematic effect which, being synchronous on the timelines, is not coincident on the maps because of the shifts between detectors.

In table 1, we give for all channels the ratio between the RMS of the signal (CMB or dust) and the error performed on its measurement with our simulation setup. The error contains contributions from detector noise, from the other astrophysical component, from the instrumental effect, and from observational errors (beam smoothing and reprojection effects).

4 IMPLEMENTATION OF A COMPONENT SEPARATION

The separation of astrophysical components we implement is possible essentially because the components have distinct emission spectra as a function of radiation wavelength. This is illustrated in figure 4. If the number of components and their respective spectra were perfectly well known, and if measurements were noiseless, multifrequency observations (with at least as many observations as there are components) would allow in principle the perfect recovery of the emission of each of the component at each point. In practice, imperfections of the measurements and the model make the problem slightly more complicated.

4.1 First principles

In the case where astrophysical components only are present, we are given a number N_ν of observations of the same sky (or fraction of sky) at different frequencies ν, each of which can be written as a linear superposition of emissions from the various astrophysical sources of radiation (CMB, dust, synchrotron, SZ...) with some noise added:

$$m_\nu(\vec{x}) = A_{\nu c} T_c(\vec{x}) + n_\nu(\vec{x}) \tag{6}$$

This equation can equivalently be written in Fourier space, as

$$m_\nu(\vec{k}) = A_{\nu c} T_c(\vec{k}) + n_\nu(\vec{k}) \tag{7}$$

$A_{\nu c}$ is the "mixing matrix" of this component separation problem, which is determined by the spectrum of the emission of the astrophysical components (up to a global calibration factor for each component) and by the optical response of the instrument.
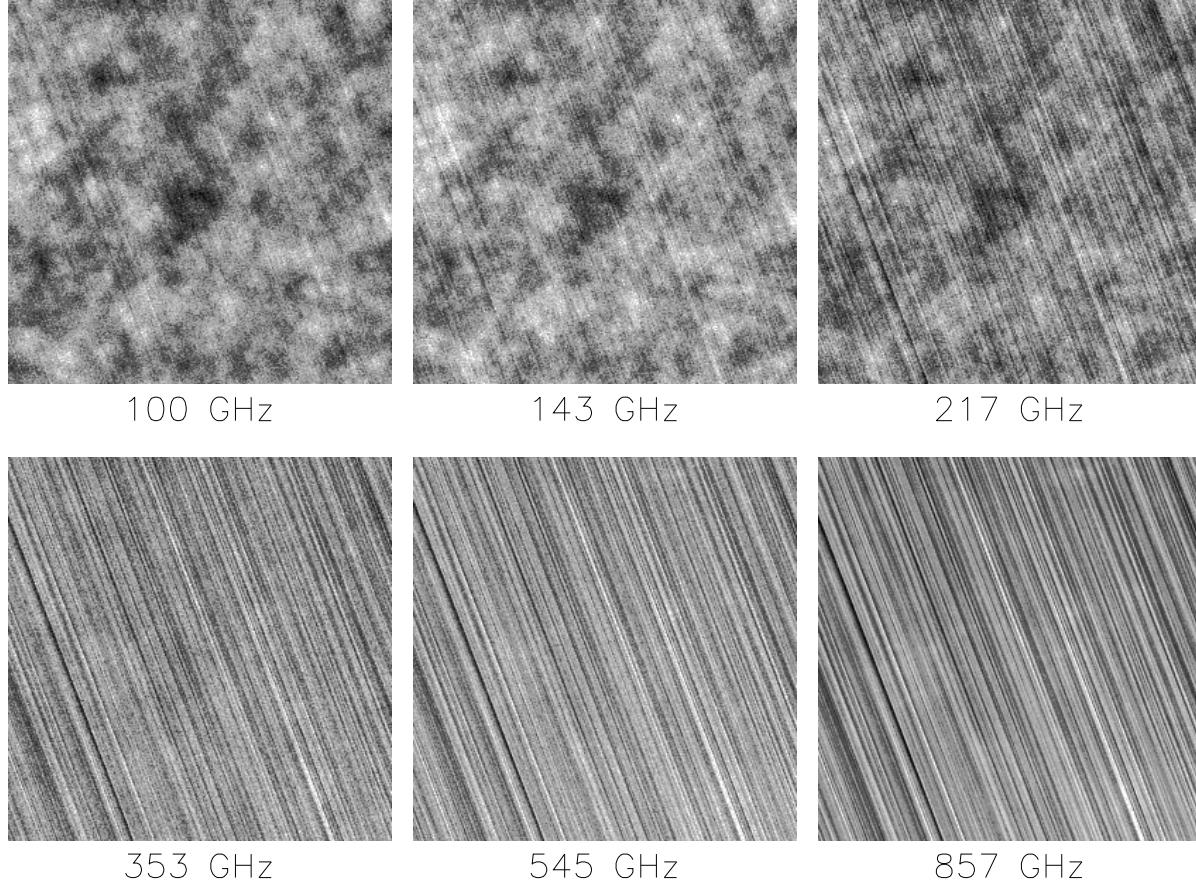
100 GHz   143 GHz   217 GHz

353 GHz   545 GHz   857 GHz

Figure 2. Observations for one detector at each wavelength. For illustrative purposes, we have chosen here a strong systematic effect, which is comparable to CMB emission at low frequencies, and dominates over dust at high frequencies.
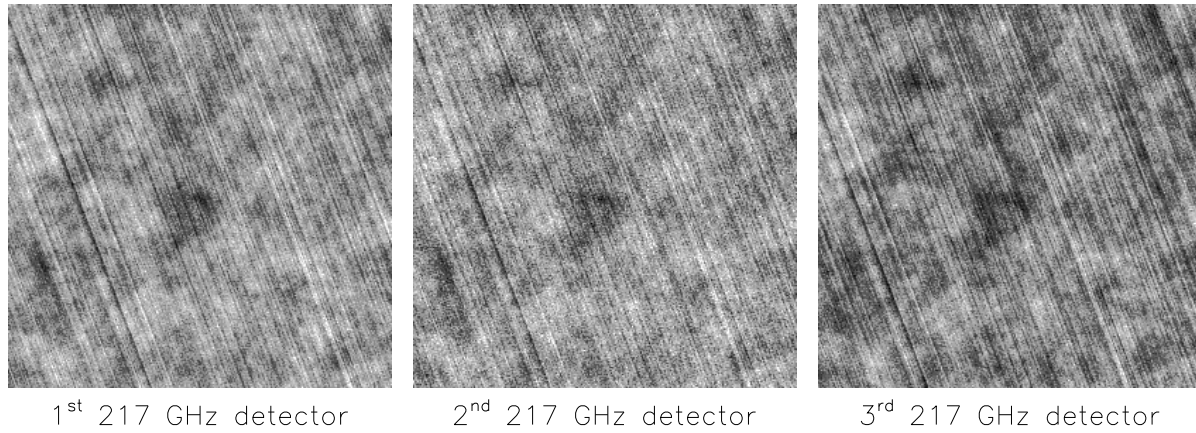

1st 217 GHz detector 2nd 217 GHz detector 3rd 217 GHz detector

Figure 3. Observations by three different detectors of the 217 GHz channel. In our example here, the observations at this frequency are dominated by CMB anisotropies and stripes induced by the instrumental effect . The detector corresponding to the middle panel is polarised and thus slightly noisier after recalibration of the observations, because half of the input power (here assumed to be unpolarised) is rejected. The increased granularity due to high frequency noise can (barely) be seen on the observation. The detector-dependent shift of the systematic effect with respect to sky emission is clearly visible on these observed maps (look at the distance of the darkest stripe to the upper left corner of the maps).

Table 1. Signal to Noise ratio for CMB and dust for observations in all channels. Here we consider as "noise" the error from all sources : detector noise, smoothing with the beam, other components, and reprojection effects.

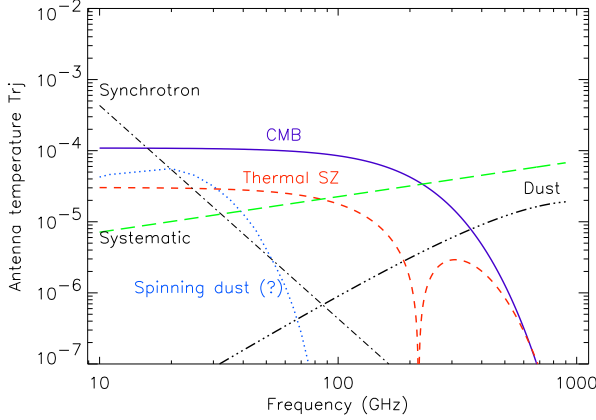| channel	100	143	143p	217	217p	353	545p	857
number of det.	4	3	9	4	8	6	8	6
S/N CMB	1.4	1.2	0.95	0.77	0.65	0.16	0.01	10^{-4}
S/N dust	8.9×10^{-3}	2.0×10^{-2}	1.7×10^{-2}	5.9×10^{-2}	5.2×10^{-2}	0.14	0.22	0.26

Figure 4. Foreground emission in the frequency range of interest, as compared to CMB anisotropy spectrum. The existence of three major galactic foregrounds, which are thermal dust emission, synchrotron, and bremsstrahlung (also called free-free, not represented here), is well established. There is some evidence towards the existence of microwave emission due to rotating dust. SZ effect generates foreground emission towards clusters of galaxies, and possibly filamentary structure between them. We have added a plausible spectrum for a systematic effect due to temperature fluctuations of an aluminium telescope mirror. Relative levels are arbitrary, so that the curve for each foreground emission can move up and down depending on the level of contamination. The assumed shape of a possible spinning dust component is from Draine & Lazarian (1998)

If there are more observing frequencies than astrophysical components, and if the distributions for n and T are Gaussian and their autocorrelations N and S are known, the Wiener solution can be written as:

$$\widetilde{T} = [S^{-1} + A^t N^{-1} A]^{-1} A^t N^{-1} m \equiv W m \qquad (8)$$

Equation 8 defines the Wiener matrix $W = [S^{-1} + A^t N^{-1} A]^{-1} A^t N^{-1}$, which gives the best estimate $\widetilde{T}$ of the sky temperature T.

4.2 Including instrumental effects

Let us now assume that a number of instrumental effects are to be added to our model. The measurement for each detector can be written as:

$$m_d(\vec{x}) = A_{dc} T_c(\vec{x}) + A'_{dz} S_z(\vec{x}, d) + n_d(\vec{x}) \qquad (9)$$

where now d indexes detectors. $S_z(\vec{x}, d)$ is the detector-dependent projection of the instrumental component. This "reprojection" of the time-dependent instrumental compo-

nent is not the same for all detectors because although all detectors experience the same instrumental effect (up to detector-dependent coupling factors) at the same time, they do not see the same pixel at the same time. Therefore, the systematic effect which pollutes the measured map in $\vec{x}$ is not the same for two different detectors d and d'. Because of this, it is not possible to recombine simply the measurements of all the detectors at a given frequency into one single map.

In all generality, $S_z(\vec{x}, d)$ depends on the scanning strategy and on the relative orientation of the focal plane and the scanning direction. Therefore the relationship between reprojected effects $S_z(\vec{x}, d)$ and $S_z(\vec{x}, d')$ between two different detectors d and d' may be far from trivial (see appendix). However, if we restrict ourself to region of the sky where all the scans are parallel, there is a constant shift $\Delta \vec{x}_d$ between the direction pointed by detector d and that of the optical axis, which is set entirely by the geometry of the image of the focal plane on the sky. In that case equation (9) can be rewriten:

$$m_d(\vec{x}) = A_{dc} T_c(\vec{x}) + A'_{dz} S_z(\vec{x} - \Delta \vec{x}_d) + n_d(\vec{x}) \qquad (10)$$

where $S_z(\vec{x})$ is now the instrumental noise projected on the sky in the direction of the telescope optical axis. Although it is not possible to average in bands without loosing information on the systematic, the system has a linear structure close to that of equation 6, except for the additionnal systematic effect.

Rewriting equation 10 in Fourier space, we get

$$m_d(\vec{k}) = A_{dc} T_c(\vec{k}) + A'_{dz} \exp(i\vec{k}.\Delta \vec{x}_d) S_z(\vec{k}) + n_d(\vec{k}) \qquad (11)$$

This has exactly the same structure as that of equation 7 if we include the spatial frequency dependent term $\exp(i\vec{k}.\Delta \vec{x}_d)$ into matrix A', and regroup matrices A and A' into one single matrix (and (T_c, S_z) into one single vector). Therefore, we can apply a Wiener method to our extended problem. There are a few technical differences with the implementation of Bouchet and Gispert (1999):

• in the present case, because of the phase shift for the systematic component, the mixing matrix A is complex;
• because of the problem asymmetry induced by the privileged scanning direction, the Wiener matrix W depends on $\vec{k}$ not simply on $|\vec{k}|$;
• the noise we assume is not white.
• we have one observed map for each detector, not one single map per frequency band.
• the observed maps are not simply the superposition of the true pixellised maps with white noise added, but are reconstructed from timelines and pointings by a global fit to the data, which takes into account some of the inaccuracies of the map-making.

4.3   Finite beam effect

The effect of symmetric finite beams is to convolve the maps with a symmetric kernel $B(\vec{x})$. For asymmetric beams, the integration of the sky in the beam is scan-direction dependent, so that the operation is not strictly a convolution, except in the case of local parallel scanning. In Fourier space, the sky temperature T_c is multiplied by the Fourier transform of the asymmetric beam pattern (properly oriented). The effect of the beam can therefore be taken straightforwardly into account by putting its $\vec{k}$-dependent effect into matrix A (but not matrix A', as the systematic effect is not affected by the shape of the beam). Each component A_{dc} of matrix A needs to be replaced in equation 11 by the product $A_{dc}B_d(\vec{k})$ (no summation), where $B_d(\vec{k})$ is the Fourier transform of the beam map for detector d. We include the effect of the symmetric Gaussian beams in the evaluation of the mixing matrix A for the inversion in Fourier space.

4.4   Implementation

The implementation of the Wiener method in Fourier space requires the apodisation of the maps to avoid border effects. We take an apodisation function which goes to zero over 15 pixels (out of 272) on each side of the map, following a sine function from $\pi/2$ to 0. This apodisation induces little smoothing on the spectrum in $\vec{k}$-space, and leaves the inner region of the map untouched.

The implementation of the Wiener solution also requires prior information of the spectrum in $\vec{k}$-space, $S(\vec{k})$, for all components. For the CMB, we assume the true underlying spectrum (which differs slightly from the actual spectrum of our realisation because of the sample variance). For dust, we assume a $1/(|\vec{k}| + C)^3$ law, where C is a constant chosen to fit best the spectrum on the IRAS map. For the systematic, we take the average of 10 realisations of a systematic according to the same generation law that we use for generating the actual observed systematic. Therefore, for all components, we assume a spectrum which is close to the reality, but not exact (either because of sample variance, or because of different realisation, or a prior empirical fit). We consider that this is representative of the uncertainty we will have when dealing with actual measurements. We discuss in more details the effect of uncertainties in the model of the measurement (and in particular uncertainties in pointing, frequency scalings) in the next section.

The simulation and inversion we implemented takes a few minutes of running time for 300×300 2.5 arcminute pixels maps, on a very modest workstation.

4.5   Results

In figure 5, we display the result of our inversion. Apart for border effects which here cannot be avoided, the original maps are well recovered. Border effects are due both to the apodisation and to discontinuity effects of the instrumental effect map. Apodisation effects appear only in a Fourier implementation, and could be avoided in real space implementations, at the cost of enormous required computation time. The discontinuity effect on the other hand is not a problem of the implementation. It appears because the map

Table 2. Final Signal to Noise ratio for CMB and dust, for both the 48-detector and the 6-detector inversions. Figures in parentheses are obtained when the output is compared with the original map smoothed with the effective beam.

component	CMB	dust
48-detector separation	7.0 (10.1)	3.5 (5.1)
6-detector separation	4.1 (5.5)	2.5 (3.7)

of the instrumental effect is not periodic, and the actual instrumental effect limited to the region of observation is thus not exactly the same for all detectors, because of detector shifts. The effect remains small as long as detector shifts are small compared to the size of the map.

The RMS error on CMB anisotropies measurement, computed as the difference between the true input CMB maps and the output map (obtained from the reprojection of timelines and suffering from convolution with the beam, additive noise, and possibly residuals of other components after the separation process) is $\Delta T/T \simeq 5.3 \times 10^{-6}$ in the central region of the map, corresponding to a signal to noise ratio of about 7.

Dust emission is very subdominant in all channels of our simulation, because we have chosen quite a strong instrumental effect. This is unlikely to be the case for Planck, but may be typical of some balloon-borne experiments. Despite of the fact dust can barely be seen in individual detector observations, its emission, in the central region, is recovered with a signal to noise ratio of about 3.5, and a $\Delta T/T$ of 5.3×10^{-7} (at 200 GHz).

For both components, final results are much better than what could be expected from simple weighted averaging of all measured maps, as is clear when comparing the final S/N rates with figures from table 1, and output maps (fig. 5 with maps of the observations 2.

The stripes due to the instrumental effect are well recovered, with a signal to noise of 7.2 in the central region of the map. Of course, the sides of the map are not recovered as well, because of both the apodisation and the non-toric geometry of our maps, which invalidates the Fourier phase shift approximation of the actual dispacement of each detector at the borders.

In table 2 we show the signal to noise ratio obtained at the end of the inversion, both for the 48-detector inversion and for a 6-detector inversion with one detector per channel only. For each case, we give S/N computed in two ways. The first way is to compute the error from the difference between the "true" input map and the recovered map. The second is to compute the error from the difference between the input map smoothed with the effective beam (see 4.6), and the recovered map. Values obtained with the second method are given in parentheses. The difference between the two is due to the part of the true astrophysical signal which is not recovered because of the imperfect resolution.

The difference between the signal to noise ratio for the 6-detector inversion and the 48-detector inversion is compatible with the loss of sensitivity due to the reduction of the number of detectors by a factor of 8.

In summary, the separation algorithm we implemented performs very satisfactorily, and can be a useful tool to con-
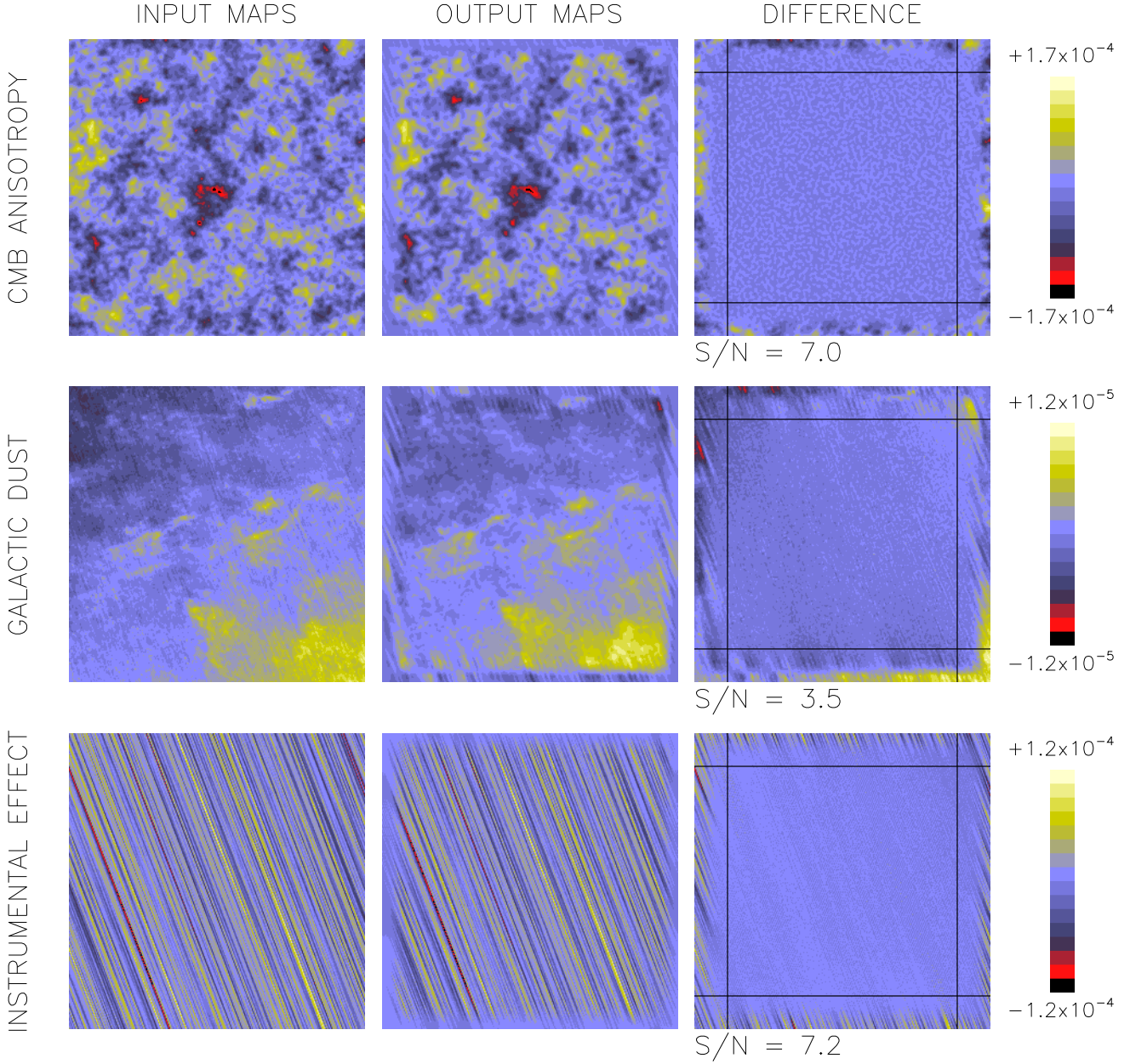
Figure 5. Results of the inversion. The input maps are displayed in the first column. Maps for CMB and dust are original maps, whereas the map for the instrumental effect is a reprojection of the effect's timeline. The output of the inversion, to be compared with the original maps, are displayed in the second column. The difference is shown in column three. For each component (on each line), the three maps are displayed with the same greyscale table (shown on the right of the figure) where figures give values for $\Delta T/T_{CMB}$ at 200 GHz. Signal to noise ratios of the final measurement in the center region (delimited by black lines on the difference maps are given below the difference maps.)

strain instrumental effects and separate various components in CMB data for a scanning experiment such as Planck.

4.6   Effective beams

As $\widetilde{T} = Wm$, we have $\widetilde{T} = WAT +$ (noise term), W being the Wiener matrix and A the mixing matrix. This permits to compute an "effective beam" for each component, which is

Table 3. Effective co-scan and cross-scan beam sizes for CMB and dust, for both the 48-detector and the 6-detector inversions.

Direction	co-scan	cross-scan
48-det. CMB effective beam	7.99 arcmin	7.99 arcmin
48-det. dust effective beam	6.83 arcmin	7.07 arcmin
6-det. CMB effective beam	10.0 arcmin	10.0 arcmin
6-det. dust effective beam	9.82 arcmin	12.9 arcmin

the backward Fourier transform of the appropriate diagonal term of $W(\vec{k})A(\vec{k})$.

The final effective beam is due to a combination of the instrumental beam (which gets into matrix A) and of the attenuation of some spatial frequencies, where noise dominates, by the Wiener filter.

We compute effective beams for CMB and dust for both the 48-detector and the 6-detector inversions. These effective beams are well fitted by two-dimensional elliptical Gaussians. Because of the stripes, which increase the effective noise term on high frequencies perpendicular to the scanning, but not parallel to the scanning, beams are slightly elongated perpendicularly to the scanning, but this is not significant for the CMB. It is quite significant for the dust (especially in the case of the six-detectors inversion). This was to be expected, since the dust emission has a frequency dependence close to that of the systematic effect and a much lower amplitude. Effective beam width for both inversions in co-scan and cross-scan directions are shown in table 3.

The effective resolution depends on the number of detectors because in the case of 6 detectors, high frequency noise starts to dominate the signal at lower $\vec{k}$ values than when 48 detectors are present, which leads to effective beam degradation because of the Wiener filtering, which weights modes with a $S/(S+N)$ factor. Results shown in this table are pessimistic for Planck, and especially so for dust because the instrumental effect, which dominates at high frequencies where dust is the highest astrophysical contribution, is quite high as compared to what is expected.

5   DISCUSSION

Our simulations have shown that parallel stripes due to the simulated systematic effect can be separated very well from astrophysical emission in the particular case we studied here. We now discuss the reasons why it works and the dependence of the result on specific assumptions.

5.1   Impact of the number of components to be separated

The test of our method as described in this paper has been done in a particularly favorable situation as far as the number of components is concerned. We have 6 channels and 48 detectors for 3 components only. The system is thus widely overconstrained. There is, however, no fundamental problem to adding more astrophysical components, as already demonstrated by Gispert and Bouchet (Bouchet & Gispert 1999). Here, we simply demonstrate the possibility to treat instrumental effects as additionnal components, provided

the inversion is made on a system encompassing all detectors, and not co-averaged frequency channels.

We have performed tests of the method with the same number of components (two astrophysical and one systematic) but with a very limited number of detectors and channels (as little as three frequency channels and six detectors), with satisfactory results.

5.2   Impact of the spectral properties of the systematic effect

The spectral properties of the astrophysical components and of the noise is an important issue regarding the separation procedure.

Let us imagine, for instance, that the systematic effect has almost the same frequency dependence as dust emission, e.g., an emission proportionnal to ν^4. This may happen for atmospheric emission in some cases of ballon-borne experiments, or in the case of Planck if some element of the spacecraft, which temperature fluctuates and which is coupled optically to the detectors, has a greybody emission with ν^2 emissivity. In this case, the frequency dependence does not help separating the two, and if all detectors were looking at the same point of the sky at the same time, there would be a very strong degeneracy between the dust and the thermal emission. The best we could do in that case would be to filter stripes out of dust maps only based on spatial properties or on statistics (loosing at the same time some high frequency in the information on dust emission, in direction perpendicular to the stripes). However, if as in the method we propose, the information concerning the different pointing direction of each detector is used, this degeneracy can be lifted to some extent.

5.3   Further developpements

The results we have presented here used a symmetric beam. However, it is straightforward to extend our procedure to an asymmetric beam. As long as scans are parallel, the effect on the maps of an asymmetric beam can be written, mathematically, as a convolution. The Fourier components of the sky emissions are multiplied by the Fourier transform of the beam (properly oriented with respect to the scanning direction), which modifies their spectra. This can be taken into account easily in the formalism of the separation, where the priors on components depend on $\vec{k}$ and not simply on $|\vec{k}|$.

The generalisation of our method to non-parallel scans is more difficult. Our component separation method as implemented here works only for parallel equidistant scans. In principle, small deviations from this assumption are not critical, as long as the deviations remain small as compared to the beam sizes. The potential problem when the scanning departs from this ideal case is not the distortion of the assumed spectra for the Wiener solution, but the accuracy of the model of a detector-dependent constant displacement which permits to write the system in the simple form of equation 11. We are currently working on relaxing the parallel-scanning assumption.

A first possible generalisation concerns a portion of the sky where two sets of parallel scans cross each other (which

is often the case in actual CMB experiment). In this case, it is possible to adapt our formalism by adding two systematic effect maps (one for each scanning direction) instead of one.

6 CONCLUSIONS

In this paper, we have investigated the possibility to use Wiener filtering to separate astrophysical components and systematic effects producing slow drifts in scanning CMB anisotropy experiments as the Planck mission. We have shown that the "component separation" formalism applied so far only to astrophysical emissions can be generalised to take into account and separate instrumental effects as well.

The algorithm we implemented is especially useful to remove systematic effects of known spectrum when there is little redundancy in the measurement for each detector channel, but high correlation between the systematic effect impact in the different detector channels. Whereas we have studied here the impact of one single systematic effect, that of slow temperature drifts of an optical element of the Planck telescope, the approach can be generalised and adapted to treat more effects, as for example one or more components due to atmospheric emission.

One of the difficulties for the application of our method is to get a good evaluation of the elements of the "mixing matrix", i.e. matrix A, for the systematic effects. For Planck, an accurate modeling associated to numerical simulations may permit to constrain these elements quite well, which may not be the case for other experiments/missions. Methods permitting to estimate simultaneously mixing matrix elements and the components themselves (Baccigalupi et al. 2000; Snoussi et al. 2001; Maino et al. 2001) can have a natural application in the context we discussed here.

REFERENCES

Baccigalupi, C. et al., 2000, MNRAS, 318, 769
Benoît, A. et al., 2001, to be published in Astroparticle Physics
Bersanelli, M. & Mandolesi, N., 2000, Astro. Lett. and Communications, 37, 171
Borrill, J., 1999, in L. Maiani, F. Melchiorri, N. Vittorio, eds., Proc. AIP Conf. 476, 3K Cosmology, New York, AIP, p. 277
Bouchet, F.R., Gispert, R., 1999, NewA, 4, 443
Bouchet, F.R., Prunet, S. and Sethi, Shiv K., 1999, MNRAS, 302, 663
Cottingham, D., 1987, PhD thesis, Princeton University, Princeton, New Jersey
de Bernardis, P., et al., 1999, New Astronomy Reviews, 43, 289
Delabrouille, J., 1998, A&A Suppl. Ser., 127, 555
Delabrouille, J., Gispert, R., Puget, J.-L. in J. Tran Than Van, Y. Giraud-Héraud, F. Bouchet, T. Damour, Y. Mellier, Proc. XXXIIIrd Rencontres de Moriond, Fundamental parameters in Cosmology. Editions Frontières, p. 261
Delabrouille, J. et al., 2000, Astro. Lett. and Communications, 37, 259
Draine, B.T. & Lazarian, A., 1998, ApJ letter, 494, L19
Ferreira, P.G. and Jaffe, A.H., 2000, MNRAS, 312, 89
Hanany, S. et al., 2000, ApJ letter, 545, L5
Hobson, M.P., et al., 1998, MNRAS, 300, 1
Hu, W. and Sugiyama, N., 1996, ApJ, 471, 542
Jungman, G., et al., 1996, Phys. Rev. D, 54, 1332
Lamarre, J.-M. et al., 2000, Astro. Lett. and Communications, 37, 161
Maino, D. et al., 2001, submitted to MNRAS (astro-ph/0108362)
Mandolesi, N. et al., 2000, Astro. Lett. and Communications, 37, 151
Schlegel, D. J., Finkbeiner, D. P. and Davies, M., 1998, ApJ, 500, 525
Seljak, U., Zaldarriaga, M. , 2000, ApJ Suppl. ser., 129, 431
Silverberg, R. F., 2000, Advances in Space Research, 26, 1401
Snoussi, H. et al., 2001, to appear in MaxEnt 2001 proceedings (astro-ph/0109123)
Sunyaev, R., Zel'dovich, Y. , 1972, Comments Astrophys. Space Phys., 4, 173
Tegmark, M. and Estathiou, G., 1996, MNRAS, 281, 1297
Vielva, P. et al., 2001, MNRAS, 326, 181
Wright, E. L., 1999, New Astronomy Reviews, 43, 257

APPENDIX A: GENERAL FORMULATION OF THE FULL SEPARATION PROBLEM

In this appendix, we write a general formalism for the separation of both sky-domain (astrophysical) and time-domain (instrumental) components for a scanning experiment.

In a scanning experiment such as those currently used for CMB mapping, it is usual to write the data stream of a given detector d as a function of time as:

$$s_t = M_{tp}I_p + n_t \qquad (A1)$$

Where s_t is the data stream for that detector (and t indexes time), I_p the brightness of a pixellised sky map in pixel p, and M_{tp} the pointing matrix, which tells us how much pixel p contributes to the data stream at time t. A summation convention is assumed over the repeated index p. n_t is a noise stream, representing random noise, which may in some cases be coloured.

From a component separation point of view, the sky brightness is the sum of several astrophysical components, $I_p = A_cT_{cp}$. Here, A_c is a single column of the "mixing matrix" of the component separation problem, corresponding to one single detector d. The full mixing matrix for all detectors is noted A_{dc}.

Putting now explicitly in the equation the detector dependence as an additionnal index d, and writing explicitely the summations to avoid confusions, we get:

$$s_{dt} = \sum_p \sum_c M_{dtp}A_{dc}T_{cp} + n_{dt} \qquad (A2)$$

For a satellite experiment as Planck, the size of matrix A_{dc} is about 100×6, and the size of matrix M_{dtp} about $100 \times 10^9 \times 10^7$, making it impractical to handle all the problems at the same time. As long as the noise of all detectors are independent, it is convenient to reproject timelines onto maps (one per detector, or possibly one per frequency channel) and then separate astrophysical components.

Instrumental effects as the one we discuss in this paper can be added to the formalism, in which case formula A2 becomes:

$$s_{dt} = \sum_p \sum_c M_{dtp}A_{dc}T_{cp} + \sum_i K_{di}x_{it} + n_{dt} \qquad (A3)$$

In this formula, M_{dtp} is the pointing matrix for detector d, A_{dc} the astrophysical component mixing matrix (which depends on the detector d essentially through the corresponding frequency channel), T_{cp} the sky emission of component

c in pixel p. x_{it} are the instrumental components (temperature fluctuations of spacecraft elements, atmospheric emission...) where i indexes components and t indexes time, and K_{di} the mixing matrix for these instrumental components, which depends on the physical couplings between the sources and the detectors. n_{dt} is the noise term.

In principle, equation A3 (just as well as equation A2) can be rewritten in the general form $s = AT + n$. The form of equation A3, however, shows more clearly the physics underlying the model.